Antti H. Niemi, Juhani Pitkäranta, and Harri Hakula. 2007. Benchmark computations on point-loaded shallow shells: Fourier vs. FEM. Computer Methods in Applied Mechanics and Engineering, volume 196, numbers 4-6, pages 894-907.

Available online at www.sciencedirect.com

Comput. Methods Appl. Mech. Engrg. 196 (2007) 894–907

Computer methods in applied mechanics and engineering

www.elsevier.com/locate/cma

Benchmark computations on point-loaded shallow shells: Fourier vs. FEM

Antti H. Niemi *, Juhani Pitkäranta, Harri Hakula

Institute of Mathematics, Helsinki University of Technology, P.O. Box 1100, FIN-02015 Hut, Finland

Received 25 April 2005; received in revised form 3 April 2006; accepted 6 July 2006

Abstract

In this paper, we study experimentally the performance of the finite element method when approximating the characteristic shell layers that arise from boundaries and load irregularities in a thin shell. For that purpose we introduce a set of model problems where the shell is under a certain periodic and self-balancing point load distribution. We use a simplified shallow shell model with constant coefficients for a thin, linearly elastic shell and apply Fourier techniques to obtain the "exact" displacement and strain fields in different geometries.
© 2006 Published by Elsevier B.V.

Keywords: Finite elements; Shells; Locking; Shell layers; Benchmark study

1. Introduction

The finite element modelling of shells is known to be a very demanding task because of the numerous parametric error amplification or locking phenomena. There seems to be two main strategies to circumvent locking in the state-of-the-art finite element models of thin shells. The traditional engineering approach is the construction of efficient but simple low-order shell elements whereas the more recent alternative is the so-called *hp*-version of the standard finite element scheme. In the present work, we will touch both aspects of the methodology.

The use of high-degree polynomials in shell modelling has been previously advocated in [1–4]. In the *hp*-methods, convergence is obtained by combining proper mesh-refinement and an increase of the degree of the polynomials. Especially the error analysis is then rather straightforward since the energy principle remains intact and even exponential convergence rates may be obtained. Although it is impossible to completely avoid locking, the effects are often mild enough considering practice when the polynomial degree is sufficiently high. The notable benefit of standard finite elements of high order is their ability to capture different shell deformations efficiently. To achieve the same level of reliability with a single low-order formulation has proven to be a major challenge. Nevertheless, there are promising attempts like the MITC-type elements that have been very successful in plate-bending problems. We consider here the MITC4 shell element and rely on the results of [5,6], where the original geometrically incompatible 3D formulation is connected to classical shell models. Indeed, the approximation of the shell geometry may be understood as purely numerical modifications of the membrane strains associated with the standard bilinear scheme for the shallow shell model. The influence of these modifications (abbreviated here as MITC4-S) is not completely analysed yet, but some results are available. It is shown in [7,8] that at least under some favourable conditions the method is relatively free of locking.

Our focus is on the locking effects of the layer components since these are not so well understood and also very harmful for an engineer when trying to resolve accurately e.g. the local stress maxima. In order to investigate the effects, we present a model problem with a concentrated

---

* Corresponding author.
E-mail address: antti.h.niemi@tkk.fi (A.H. Niemi).

0045-7825/$ - see front matter © 2006 Published by Elsevier B.V.
doi:10.1016/j.cma.2006.07.012

point load so that a point layer ("hot spot") is generated at the load application point. If the shell geometry is of parabolic or hyperbolic nature, then also strong line layers appear decaying from the characteristic lines through the hot spot. Utilizing Fourier techniques, we then give a procedure to obtain reference solutions of arbitrary precision. In particular, we analyze numerically the performance of standard high-order finite elements and the MITC4-S formulation in model cases involving different shell geometries. The results confirm the robustness of standard high-order finite elements and show that the numerical modifications in MITC4-S improve the standard bilinear scheme considerably also when approximating layers. We point out that in our experiments, the underlying mathematical model is exactly the same for the analytical and finite element solutions.

The paper is organized as follows. In Section 2 we specify the simplified shallow shell model and give a brief review of the existing theory of the numerical locking effects in the FEM approximation of shell deformations. The model problem is introduced and analyzed in Section 3 whereas Section 4 is devoted to benchmark computations in selected test cases.

2. The linear shell problem

The starting point for our study is a dimensionally reduced linear shell model of Reissner–Naghdi type for a shell consisting of homogeneous isotropic material with Poisson ratio ν. The deformation of the shell is described in terms of a displacement field $\boldsymbol{u} = (u, v, w, \theta, \psi)$ defined on the shell midsurface ω. In addition to the tangential displacements u, v and the transverse displacement w, the vector field $\boldsymbol{u}$ consists of the dimensionless rotations θ, ψ related to the transverse shear deformations.

2.1. The mathematical shell model

In our model the scaled strain energy of the shell with a constant thickness t may be expressed as

$$\mathscr{A}(\boldsymbol{u},\boldsymbol{u}) = \mathscr{A}_{\mathrm{m}}(\boldsymbol{u},\boldsymbol{u}) + \mathscr{A}_{s}(\boldsymbol{u},\boldsymbol{u}) + t^2\mathscr{A}_{\mathrm{b}}(\boldsymbol{u},\boldsymbol{u}). \tag{1}$$

The different bilinear forms represent the portions of energy stored in membrane, transverse shear and bending deformations. They are defined as

$$\begin{aligned}\mathscr{A}_{\mathrm{m}}(\boldsymbol{u},\boldsymbol{u}) &= \int_\omega \left\{\nu(\beta_{11}+\beta_{22})^2 + (1-\nu)(\beta_{11}^2 + 2\beta_{12}^2 + \beta_{22}^2)\right\}\mathrm{d}\omega,\\ \mathscr{A}_{s}(\boldsymbol{u},\boldsymbol{u}) &= \frac{1-\nu}{2}\int_\omega \{\rho_1^2+\rho_2^2\}\mathrm{d}\omega,\\ \mathscr{A}_{\mathrm{b}}(\boldsymbol{u},\boldsymbol{u}) &= \frac{1}{12}\int_\omega \left\{\nu(\kappa_{11}+\kappa_{22})^2 + (1-\nu)(\kappa_{11}^2 + 2\kappa_{12}^2 + \kappa_{22}^2)\right\}\mathrm{d}\omega,\end{aligned} \tag{2}$$

where β_{ij}, ρ_i, and κ_{ij} are the membrane, transverse shear, and bending strains, respectively.

In the following we will simplify the model by assuming that ω is a rectangular domain expressed in the coordinates x and y. Furthermore, we assume that the curvature tensor $\{b_{ij}\}$ of the midsurface is constant and write $a = b_{11}$, $b = b_{22}$, and $c = b_{12} = b_{21}$. The shell is then called elliptic when $ab - c^2 > 0$, parabolic when $ab - c^2 = 0$, and hyperbolic when $ab - c^2 < 0$.

The above assumptions are valid for example when the shell is shallow, i.e. the midsurface differs only slightly from a plane. In general the strain fields in Eq. (2) depend on the geometry of the shell. In the simplest case one may set $\mathrm{d}\omega = \mathrm{d}x\,\mathrm{d}y$ and write the relation between the strain and the displacement fields as

$$\begin{aligned}&\beta_{11} = \frac{\partial u}{\partial x} + aw, \quad \beta_{22} = \frac{\partial v}{\partial y} + bw, \quad \beta_{12} = \frac{1}{2}\left(\frac{\partial u}{\partial y} + \frac{\partial v}{\partial x}\right) + cw,\\ &\rho_1 = \theta - \frac{\partial w}{\partial x}, \quad \rho_2 = \psi - \frac{\partial w}{\partial y},\\ &\kappa_{11} = \frac{\partial \theta}{\partial x}, \quad \kappa_{22} = \frac{\partial \psi}{\partial y}, \quad \kappa_{12} = \frac{1}{2}\left(\frac{\partial \theta}{\partial y} + \frac{\partial \psi}{\partial x}\right).\end{aligned} \tag{3}$$

It turns out that this simplified model preserves all the basic features of the shell problem from the numerical modelling point of view. For more details (and a rigorous justification) of the model, see [9].

If $\mathscr{L}$ is a linear functional corresponding to the potential energy of the external load, then according to the energy principle the deformation of the shell is obtained by minimizing the total energy

$$\mathscr{F}(\boldsymbol{u}) = \frac{1}{2}\mathscr{A}(\boldsymbol{u},\boldsymbol{u}) - \mathscr{L}(\boldsymbol{u}) \tag{4}$$

over the kinematically admissible displacements $\boldsymbol{u} \in \mathscr{U}$. The energy space $\mathscr{U}$ consists of displacement fields $\boldsymbol{u}$ such that the strain energy of the shell is finite and the given kinematic constraints are satisfied. The problem is then well-posed provided that u, v, w, θ, ψ along with the first partial derivatives are square integrable, $\mathscr{L}$ is bounded on $\mathscr{U}$, and the kinematic constraints are strong enough to prevent rigid body motions.

2.2. Shell asymptotics and layer effects

A study of shell asymptotics is necessary to shed some light on the various locking phenomena observed in the numerical modelling of thin shell structures. The asymptotic behaviour of shells is known to be very case-specific depending on the geometry of the shell, the kinematic constraints, and the applied load. Shell problems are usually classified based on which type of deformation energy (if any) becomes dominant at the asymptotic limit $t \to 0$ when the load is fixed. As the transverse shear energy is known to vanish asymptotically, there are two main states of deformation, namely, a *membrane-dominated* and a *bending-dominated* deformation state. The contrast between these two states is extremely sharp from the numerical point of view.

A bending-dominated deformation is kinematically possible if the boundary conditions are weak enough to allow *inextensional* displacements $\boldsymbol{u}$ that satisfy the *membrane constraints*

$$\beta_{11}(\boldsymbol{u}) = \beta_{22}(\boldsymbol{u}) = \beta_{12}(\boldsymbol{u}) = 0. \tag{5}$$

If the external load is able to excite such displacements, the asymptotic solution at $t = 0$ is also inextensional. For a small $t > 0$ the shell problem is then close to a constrained minimization problem subject to the membrane constraints (5) and to the more usual shear constraints

$$\rho_1(\boldsymbol{u}) = \rho_2(\boldsymbol{u}) = 0. \tag{6}$$

In engineering shell structures pure bending is often prevented by the boundary conditions regardless of the external load. The asymptotic behaviour of the shell is then mainly characterized by the so-called *membrane theory*, which is obtained by setting $\rho_i = \kappa_{ij} = 0$ in the energy formulation. However, in order for the shell to control the external load by means of membrane deformations only, the regularity conditions on $\boldsymbol{u}$ must be consequently relaxed. When the asymptotic solution does not obey the original boundary conditions, the solution at a small $t > 0$ contains a *boundary layer*. The situation is similar with concentrated point or line loads.

In a general problem setting it is useful to assume a splitting of the form

$$\boldsymbol{u} = \boldsymbol{u}_{\mathrm{b}} + \boldsymbol{u}_{\mathrm{m}} + \boldsymbol{u}_{\mathrm{l}}, \tag{7}$$

where $\boldsymbol{u}_{\mathrm{b}}$, $\boldsymbol{u}_{\mathrm{m}}$ are bending- and membrane-dominated fields and $\boldsymbol{u}_{\mathrm{l}}$ is the layer term. The fields $\boldsymbol{u}_{\mathrm{b}}$, $\boldsymbol{u}_{\mathrm{m}}$ are considered to be uniformly smooth with respect to t whereas the specific nature of $\boldsymbol{u}_{\mathrm{l}}$ is quite complicated and depends on the shell geometry. The layer effects are analyzed in the context of the mathematical shell model by a Fourier mode analysis in [9]. The main layer modes appear as exponentially decaying solutions to the homogeneous shell equations, the length scale of decay varying as

$$L \sim t^{1/n}, \quad n \in \{1, 2, 3, 4\}. \tag{8}$$

The case $n = 1$ is actually present also in the Reissner–Mindlin plate-bending model whereas the larger length scales are results of curvature effects. The case $n = 2$ may occur in all shell geometries and is often cited as "the simple edge effect" in the engineering literature. The length scales with $n = 3$ and $n = 4$ are possible only in hyperbolic and parabolic geometries, respectively, when the layer decays from a characteristic line of the shell midsurface.

2.3. The standard finite element scheme

In the standard finite element scheme one minimizes the total energy (4) as given in a finite-dimensional subspace of $\mathscr{U}$. The most natural error indicator is then the relative error in the energy norm

$$\mathscr{E}(\boldsymbol{u}) = \frac{|||\boldsymbol{u} - \boldsymbol{u}_{h,p}|||}{|||\boldsymbol{u}|||}, \tag{9}$$

where $\boldsymbol{u}_{h,p}$ denotes the finite element approximation of $\boldsymbol{u}$ with maximal mesh spacing h and polynomial degree p. When resolving smooth deformations in the length scale L, the optimal error bound is then $\mathscr{E}(\boldsymbol{u}) = \mathscr{O}((h/L)^p)$ by the standard finite element theory. In the present situation the error may, however, be amplified by a *locking factor* $K(\boldsymbol{u})$ as the energy norm contains a strong dependence of the thickness parameter t. The factor K is case-specific and it may even grow without a limit as $t \to 0$.

The exact value of K is well known when approximating smooth bending- or membrane-dominated deformations. We may assume that in the splitting (7) the components $\boldsymbol{u}_{\mathrm{b}}$ and $\boldsymbol{u}_{\mathrm{m}}$ are smooth e.g. in the curvature length scale $R = (a^2 + b^2 + 2c^2)^{-1/2}$, in which case we have [1–3]

$$K(\boldsymbol{u}_{\mathrm{b}}) \sim \frac{R}{t}, \qquad K(\boldsymbol{u}_{\mathrm{m}}) \sim 1. \tag{10}$$

The standard finite element scheme is thus indeed an optimal scheme in the case of a smooth membrane-dominated deformation. On the other hand, the performance deteriorates tremendously when a bending-dominated deformation is considered. This occurs because as $t \to 0$, the constraints (5) and (6) are gradually forced in the finite element subspace causing degradation of accuracy.

Perhaps less known is that significant error amplification can take place also when resolving the various boundary or interior layer components. These locking effects may be analyzed by a proper scaling of the coordinates and the displacement amplitudes so that the layer mode is seen essentially as a smooth function in the unit scale. The parametric dependence appears then more transparently as coefficients in the (scaled) energy density. The scaling is performed in [9] and it is also shown that when approximating any of the main layer modes, the error is amplified by a factor

$$K(\boldsymbol{u}_{\mathrm{l}}) \sim \frac{L}{t}, \tag{11}$$

where L is one of the length scales of decay given by Eq. (8) characteristic to the layer mode.

The parametric error amplification is most harmful to the simplest linear or bilinear finite element schemes as the convergence is typically totally ruined also for practical values of t. But, then again, even a modest raising of the polynomial degree p can substantially reduce the need for mesh-refinement.

2.4. The reduced strain finite element scheme

In the low-order approach to numerical modelling of shell structures one tries to prevent locking by a clever modification of the bilinear form $\mathscr{A}$. We assume here that the finite element mesh is a rectangular subdivision of ω aligned with the coordinates and modify the membrane strains as

$$\beta_{11} \hookrightarrow \Pi_x \beta_{11}, \quad \beta_{22} \hookrightarrow \Pi_y \beta_{22}, \quad \beta_{12} \hookrightarrow \Pi_{xy} \beta_{12}, \tag{12}$$

and the shear strains as

$$\rho_1 \hookrightarrow \Pi_x \rho_1, \quad \rho_2 \hookrightarrow \Pi_y \rho_2. \tag{13}$$

The reduction operators Π_x, Π_y, Π_{xy} are defined elementwise as averaging operators in the coordinate direction indicated by the subscript. In the finite element model, there are many other interpretations as well. The reductions may be carried out by applying appropriate interpolation or selective underintegration when evaluating the integrals involved in the forms $\mathscr{A}_{\mathrm{m}}$ and $\mathscr{A}_s$. In fact, the above variational crime was analyzed in the case of a bending-dominated cylindrical shell already in [1]. In [6], it is shown that the modifications (12) and (13) lead more generally to a scheme which is (nearly) equivalent to the MITC4 shell element of Bathe and Dvorkin, see also [10] and the references therein.

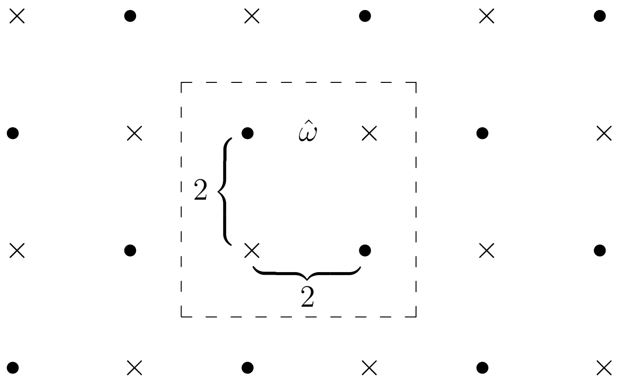

Fig. 1. Periodic point loading: (●) ~ ‘upwards’, (×) ~ ‘downwards’.

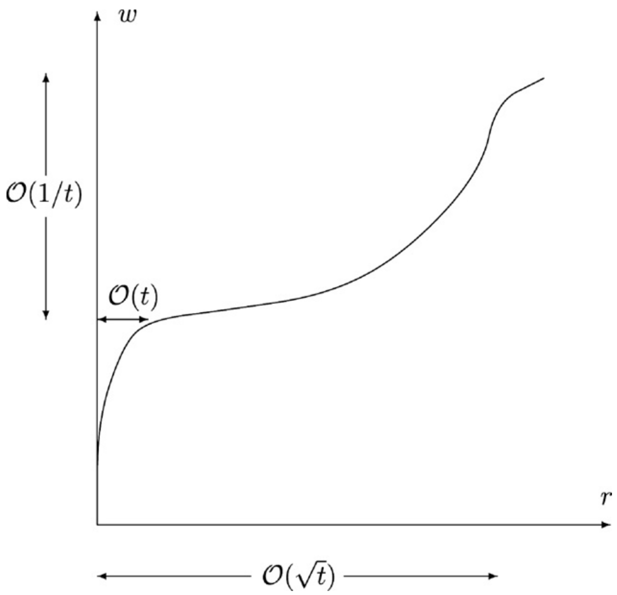

Fig. 2. The transverse displacement of a shell midsurface near a point load.

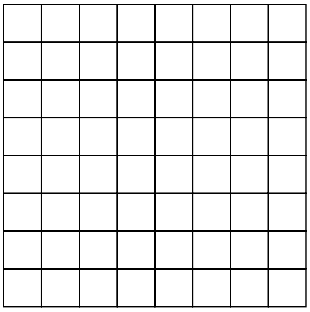

Fig. 4. Uniform mesh.

In the convergence analysis of the method, the error indicator (9) is redefined as

$$\mathscr{E}_h(\boldsymbol{u}) = \frac{|||\boldsymbol{u}-\boldsymbol{u}_h|||_h}{|||\boldsymbol{u}|||}, \tag{14}$$

where $|||\cdot|||_h$ denotes the modified energy seminorm. The results of [7,8] show then that the optimal convergence rate $\mathcal{O}(h/L)$ (with respect to the indicator (14)) is achievable when resolving smooth bending- or membrane-dominated deformations. However, this requires strong assumptions on the mesh, boundary conditions, and the regularity of the exact solution. Moreover, when the layers are taken into account, the performance of the algorithm is not so clear.

3. The model problem

3.1. The point load problem

We consider a model problem such that the shell is loaded in the transverse direction with a periodic and self-balancing point load of the form

$$f = -F\sum_{i,j}(-1)^{i+j}\delta(x-2i)\delta(y-2j), \tag{15}$$

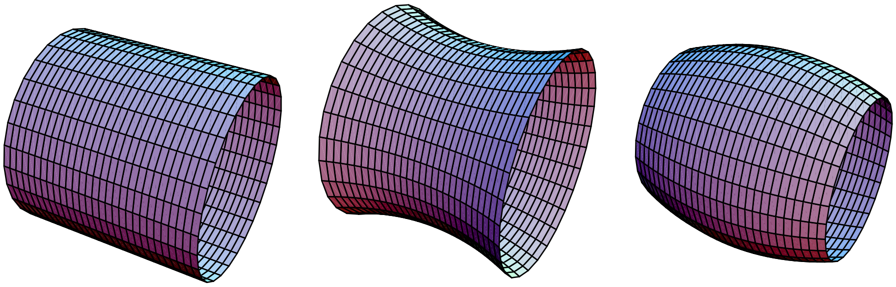

Fig. 3. Different shell geometries: parabolic (Case 1), hyperbolic (Cases 2A, B, C), and elliptic (Case 3).

Table 1
Convergence of the membrane energy in $\widetilde{\mathscr{E}}$ with respect to p

(p, N)	Case 1	Case 2A	Case 2B	Case 2C	Case 3
$(1, 32)$	7.950×10^{-1}	7.225×10^{-1}	4.298×10^{0}	6.592×10^{-1}	6.804×10^{-1}
$(2, 18)$	7.967×10^{-2}	1.267×10^{-1}	4.473×10^{-1}	1.371×10^{-1}	1.673×10^{-1}
$(4, 11)$	1.581×10^{-2}	3.488×10^{-2}	1.691×10^{-2}	2.257×10^{-2}	4.520×10^{-2}
$(8, 6)$	2.235×10^{-3}	5.451×10^{-3}	1.938×10^{-3}	4.086×10^{-3}	7.670×10^{-3}

Table 2
Convergence of the bending energy in $\widetilde{\mathscr{E}}$ with respect to p

(p, N)	Case 1	Case 2A	Case 2B	Case 2C	Case 3
$(1, 32)$	9.350×10^{-1}	9.353×10^{-1}	9.816×10^{-1}	9.264×10^{-1}	9.215×10^{-1}
$(2, 18)$	2.758×10^{-1}	4.124×10^{-1}	6.190×10^{-2}	4.205×10^{-1}	5.254×10^{-1}
$(4, 11)$	1.221×10^{-1}	1.885×10^{-1}	1.817×10^{-2}	2.103×10^{-1}	2.616×10^{-1}
$(8, 6)$	8.176×10^{-2}	1.290×10^{-1}	1.206×10^{-2}	1.409×10^{-1}	1.797×10^{-1}

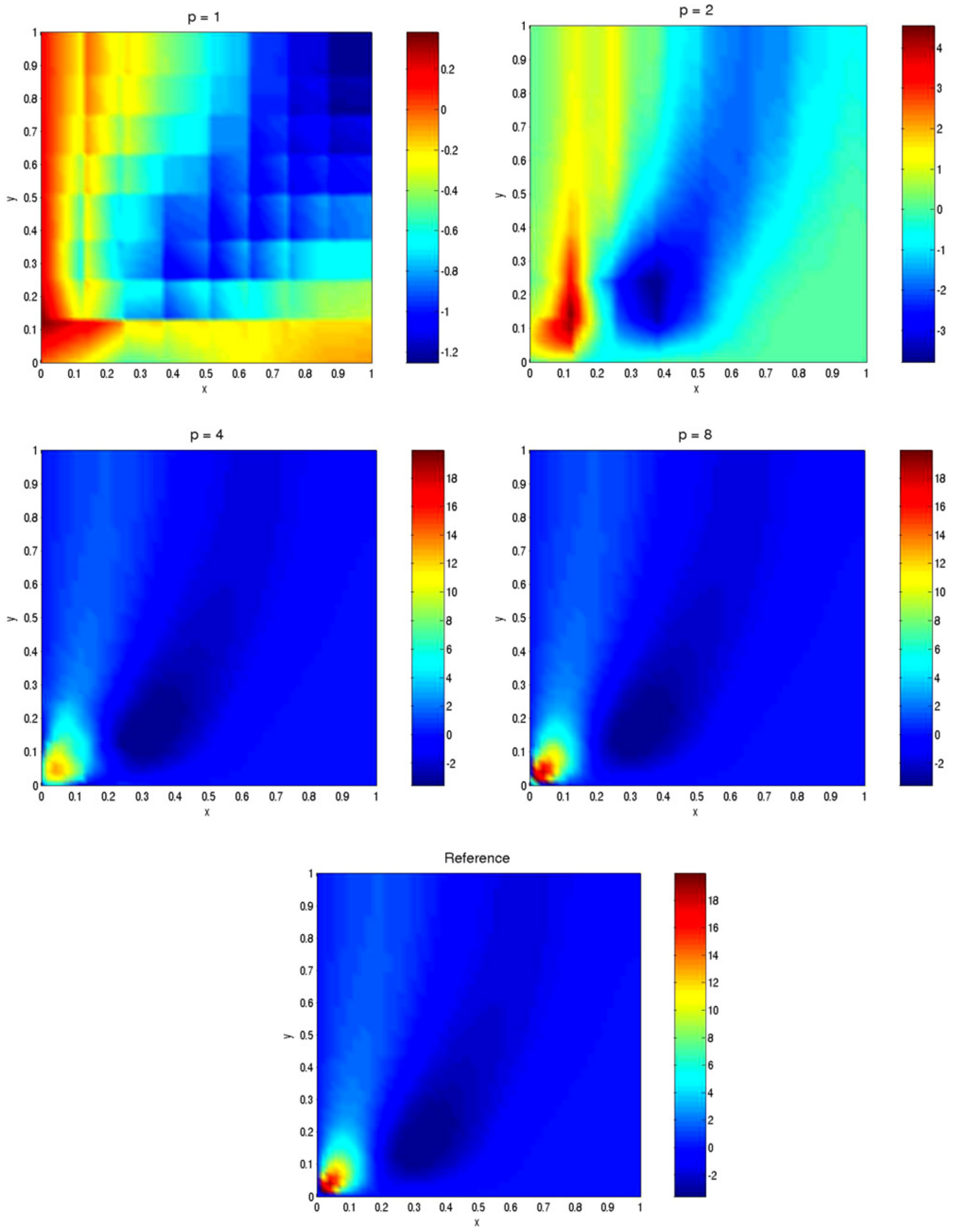
p = 1

p = 2

p = 4

p = 8

Reference

Fig. 5. The strain field e_{12} in the Case 1.

where the load amplitude $F > 0$ is a constant (Fig. 1). The corresponding linear functional is then given by

$$\mathscr{L}(\boldsymbol{u}) = -F\sum_{i,j}(-1)^{i+j}w(2i,2j). \tag{16}$$

The proposed problem may be regarded as a generalization of the classical pinched cylinder benchmark test where two normal and equal point loads are applied centrally at the opposite sides of a cylindrical surface. The quality of approximate solutions is often measured by only comparing the transverse displacement under the point load to some reference value. We would like to point out that this can be misleading since the exact value of the transverse deflection is infinite at the load application points if Reissner–Mindlin type kinematical assumption is made in the underlying shell model. Indeed, in our case the solution may be splitted as

$$\boldsymbol{u} = \boldsymbol{u}_0 + \boldsymbol{u}_1, \tag{17}$$

where $\boldsymbol{u}_1 = (0, 0, w_1, 0, 0)$ satisfies (in the distributional sense)

$$-\frac{1-\nu}{2}\Delta w_1 = f, \tag{18}$$

so that w_1 contains a logarithmic singularity at each load application point. This pinch-through is associated to locally infinite shear energy as the gradient ∇w_1 is not square

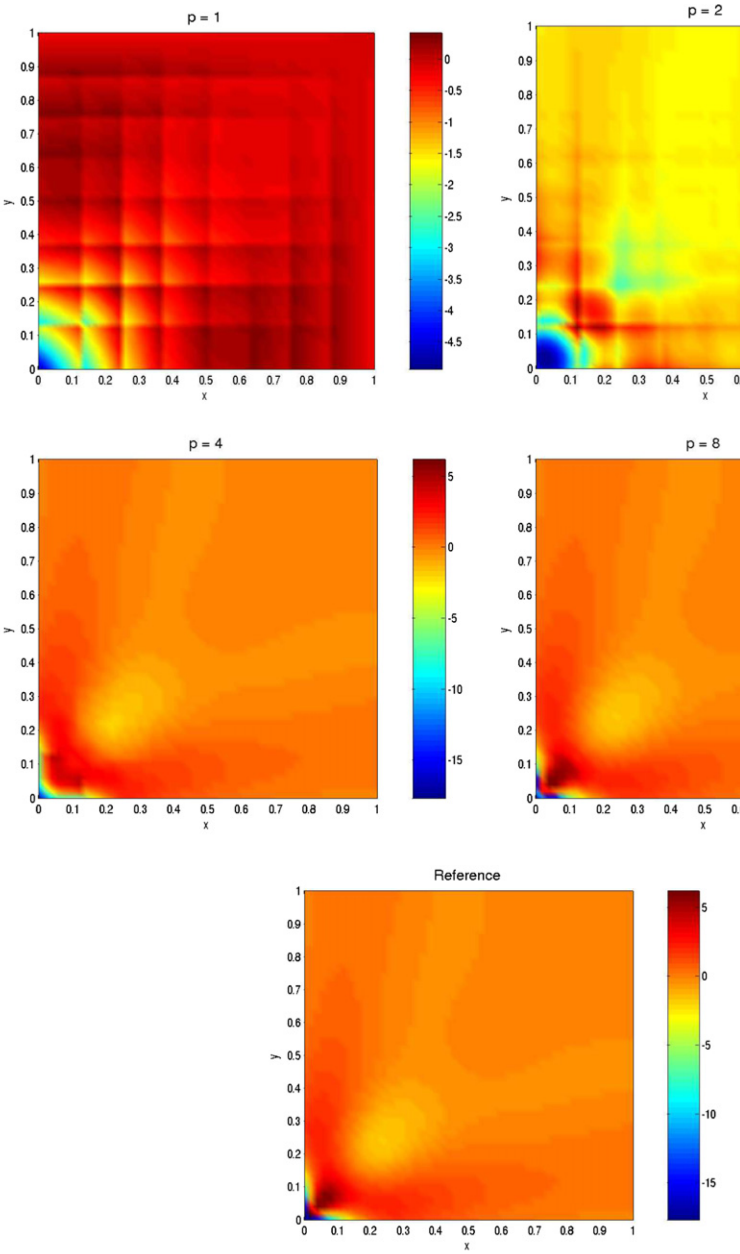

Fig. 6. The strain field e_{12} in the Case 2A.

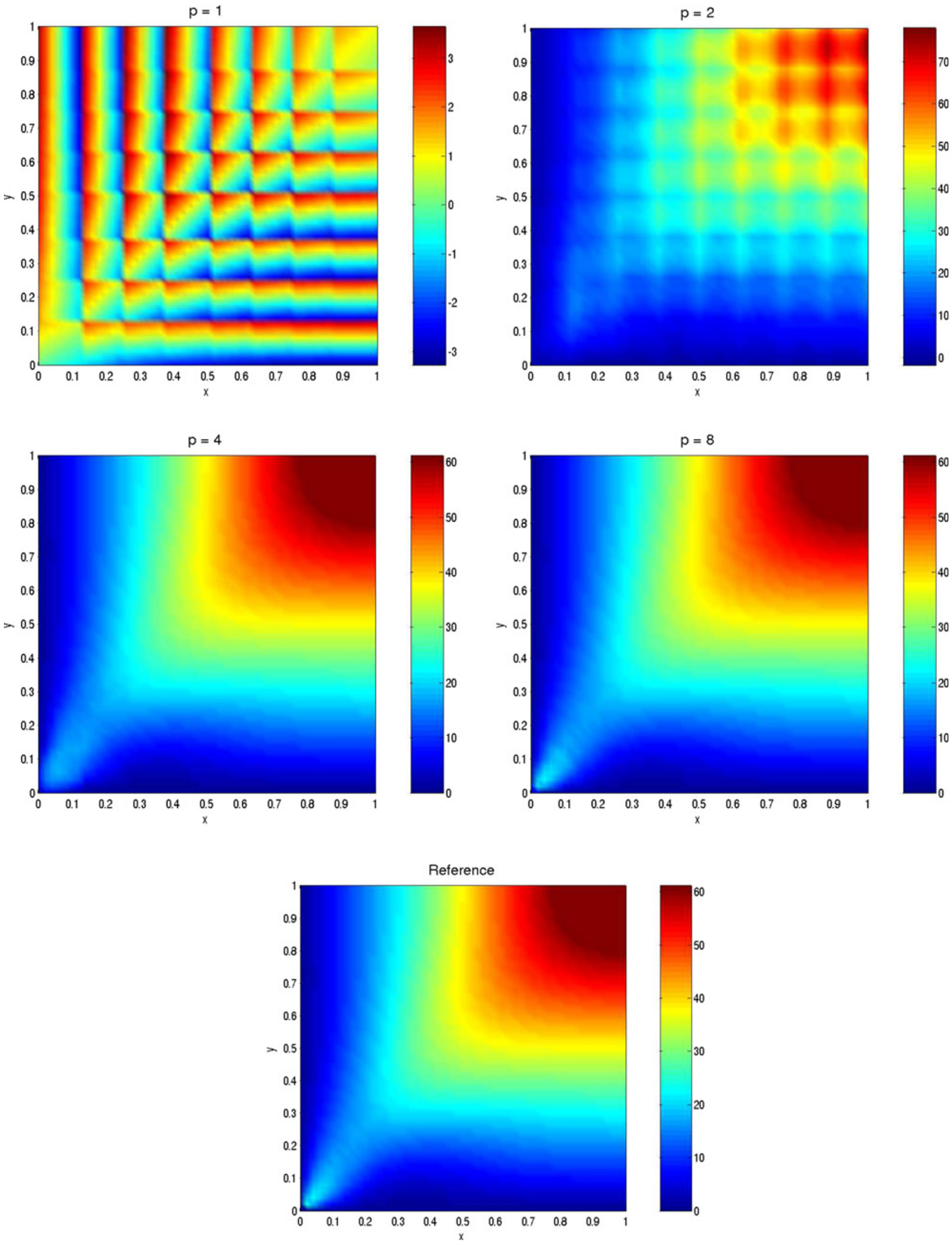

Fig. 7. The strain field e_{12} in the Case 2B.

integrable. The remaining part $\boldsymbol{u}_0$ is more regular and solves the minimization problem

$$\frac{1}{2}\mathscr{A}(\boldsymbol{u},\boldsymbol{u}) - \mathscr{A}_{\mathrm{m}}(\boldsymbol{u}_1,\boldsymbol{u}) + \frac{1-\nu}{2}\int_{\omega}\nabla w_1\cdot\boldsymbol{\theta}\,\mathrm{d}x\,\mathrm{d}y = \min!, \tag{19}$$

where we have denoted $\boldsymbol{\theta} = (\theta,\psi)$. The field $\boldsymbol{u}_0$ is actually closely related to the classical solution according to Koiter model neglecting transverse shear strains. With this simplification the bending strain expressions are reduced to

$$\kappa_{11} = \frac{\partial^2 w}{\partial x^2},\quad \kappa_{22} = \frac{\partial^2 w}{\partial y^2},\quad \kappa_{12} = \frac{\partial^2 w}{\partial x\partial y},$$

and the strain energy is given by (1) and (2) with $\rho_1 = \rho_2 = 0$ and β_{ij} as in (3).

To get a mental picture of the solution near a point load, we write down the Euler equations of the energy minimization for the Koiter model as

$$\begin{cases} 0 = -\dfrac{\partial\beta_{11}}{\partial x} - \nu\dfrac{\partial\beta_{22}}{\partial x} - (1-\nu)\dfrac{\partial\beta_{12}}{\partial y}, \\ 0 = -\nu\dfrac{\partial\beta_{11}}{\partial y} - \dfrac{\partial\beta_{22}}{\partial y} - (1-\nu)\dfrac{\partial\beta_{12}}{\partial x}, \\ f = (a+\nu b)\beta_{11} + (\nu a + b)\beta_{22} + 2(1-\nu)c\beta_{12} + \frac{t^2}{12}\Delta^2 w_K, \end{cases} \tag{20}$$

and expand the transverse displacement near the origin formally as

$$w_K = -\frac{3r^2}{2\pi t^2}\log r + \frac{r^6}{32\pi R_{\mathrm{eff}}^2 t^4}\log r + \cdots \tag{21}$$

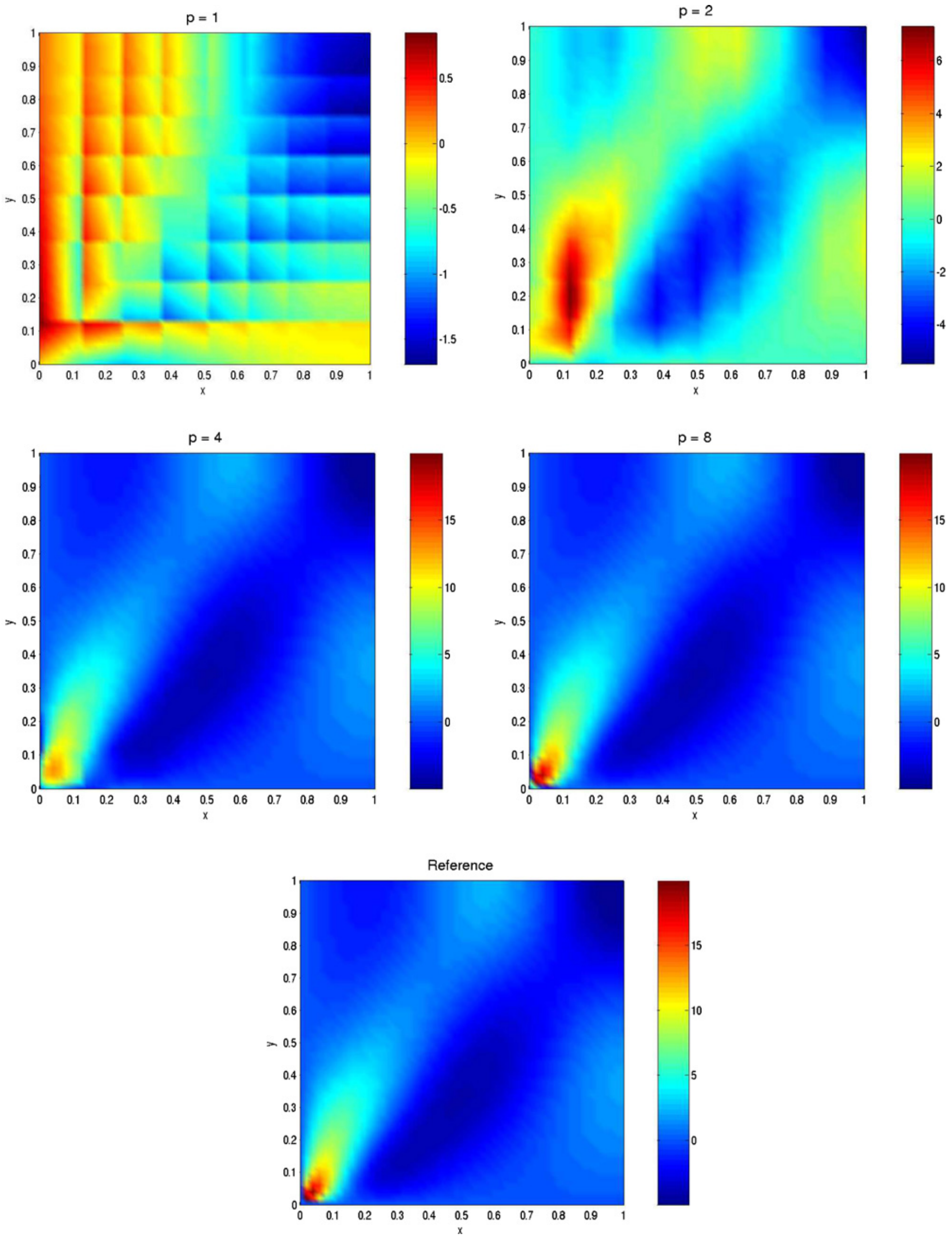

Fig. 8. The strain field e_{12} in the Case 2C.

Here r denotes the distance from the origin and the dropped terms are of higher order in r. The first term in this expansion is actually the same for a flat plate and the shell geometry manifests itself in the second term as the *effective curvature*

$$R_{\text{eff}} = \{a^2 + b^2 + 2c^2 + 2\nu(ab - c^2)\}^{-1/2}. \tag{22}$$

This reasoning suggests that a shell under a point load behaves essentially like a plate at distances $r \ll \sqrt{R_{\text{eff}} t}$ whereas the curvature effects kick in at $r \sim \sqrt{R_{\text{eff}} t}$. The specific geometry of the shell starts to play a more decisive role when $r \gg \sqrt{R_{\text{eff}} t}$, see the sections ahead.

What comes to the displacement amplitudes, we observe that w_K produces a depression of order $\mathcal{O}(1/t)$ to the transverse displacement profile. The relative supplement arising from the singular part w_1 is thus only of order $t \log h$ in a bilinear finite element model so that the 'singularity' is practically invisible.

We sum up the above development in the schematic Fig. 2 where the profile of the transverse displacement near a point load is shown and note that resolving the local behaviour of the solution exactly is an interesting mathematical problem perhaps worth a further study.

3.2. The exact solution

Taking into account the strain expressions (3) and the specific nature of the load potential (16), we conclude that in general the displacement field is of the form

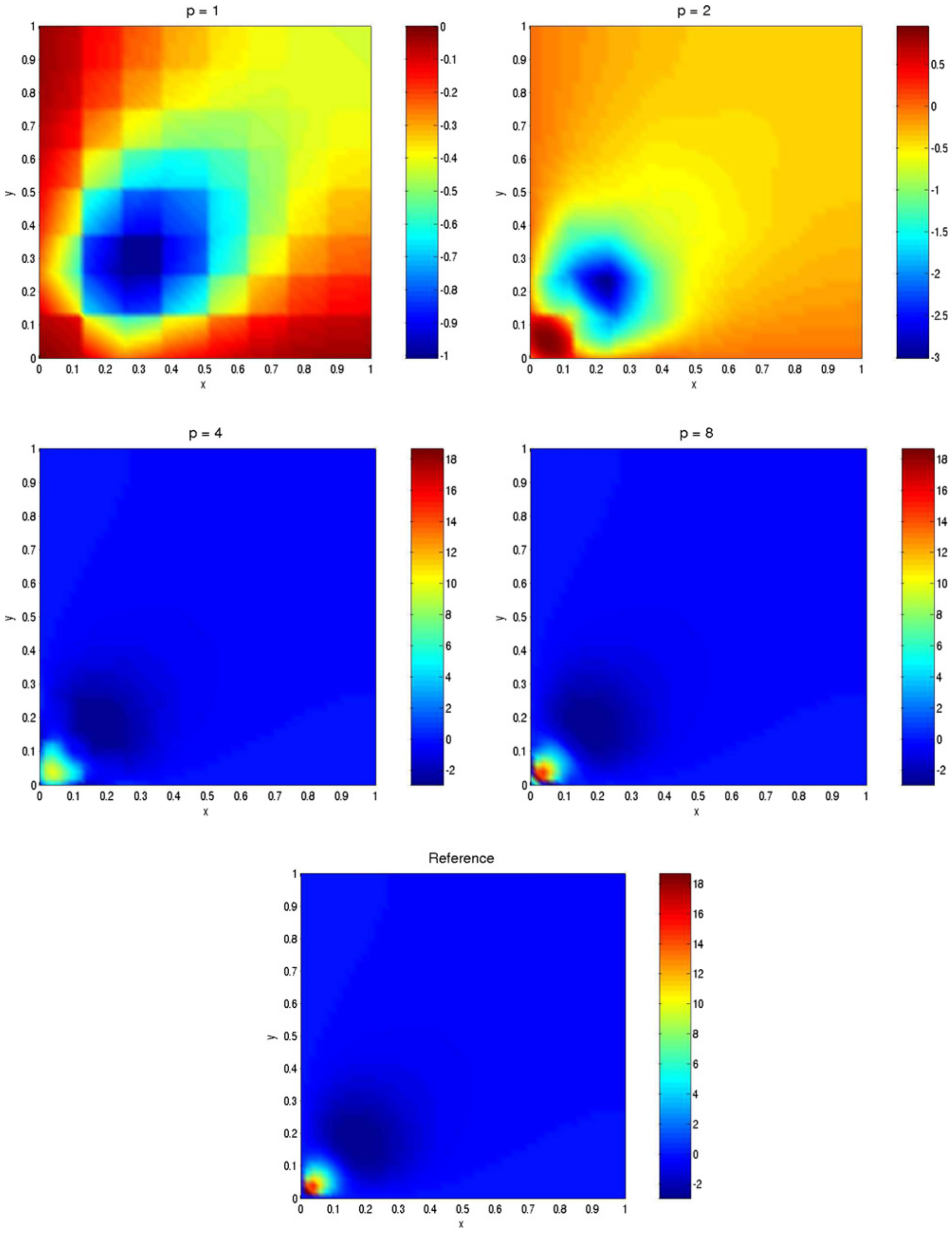

Fig. 9. The strain field e_{12} in the Case 3.

Table 3
Convergence of the membrane energy in $\widetilde{\mathscr{E}}$ using the MITC4-S formulation

N	Case 1	Case 2A	Case 2B	Case 2C	Case 3
4	2.886×10^{-1}	3.315×10^{-1}	5.729×10^{-1}	3.737×10^{-1}	4.457×10^{-1}
8	5.623×10^{-2}	1.618×10^{-1}	2.848×10^{-1}	1.666×10^{-1}	2.277×10^{-1}
16	6.571×10^{-3}	8.316×10^{-2}	1.380×10^{-1}	7.684×10^{-2}	1.106×10^{-1}
32	8.097×10^{-3}	4.157×10^{-2}	6.795×10^{-2}	3.637×10^{-2}	5.416×10^{-2}

Table 4
Convergence of the bending energy in $\widetilde{\mathscr{E}}$ using the MITC4-S formulation

N	Case 1	Case 2A	Case 2B	Case 2C	Case 3
4	2.328×10^{-1}	5.694×10^{-1}	1.174×10^{-1}	7.245×10^{-1}	7.078×10^{-1}
8	2.409×10^{-1}	3.884×10^{-1}	5.239×10^{-2}	5.064×10^{-1}	5.170×10^{-1}
16	1.497×10^{-1}	2.329×10^{-1}	2.280×10^{-2}	2.975×10^{-1}	3.201×10^{-1}
32	8.523×10^{-2}	1.323×10^{-1}	9.680×10^{-3}	1.651×10^{-1}	1.834×10^{-1}

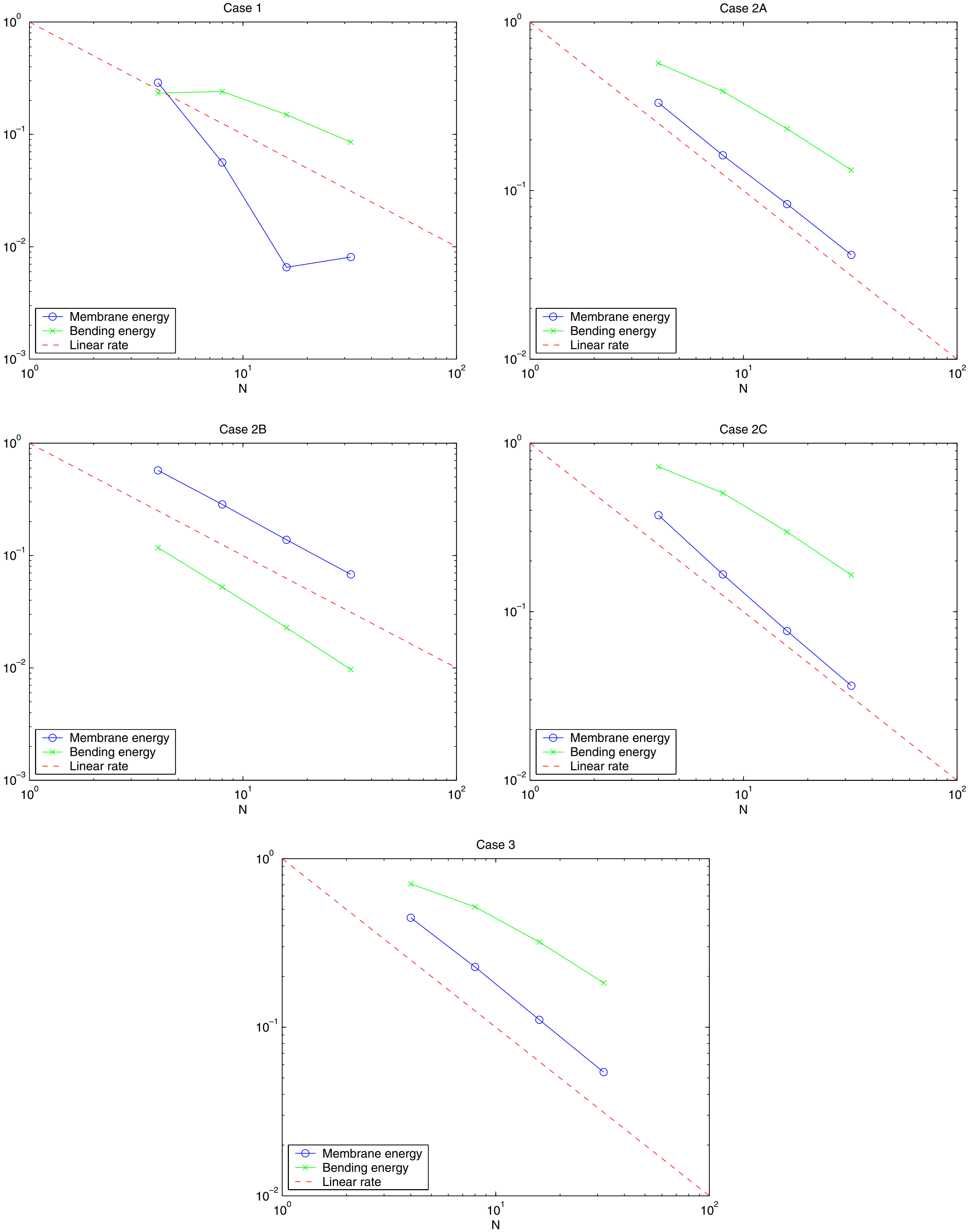

Fig. 10. Convergence of the membrane and bending energies in $\widetilde{\mathscr{E}}$ using the MITC4-S formulation and a sequence of uniform $N \times N$-meshes with $N = 4, 8, 16, 32$.

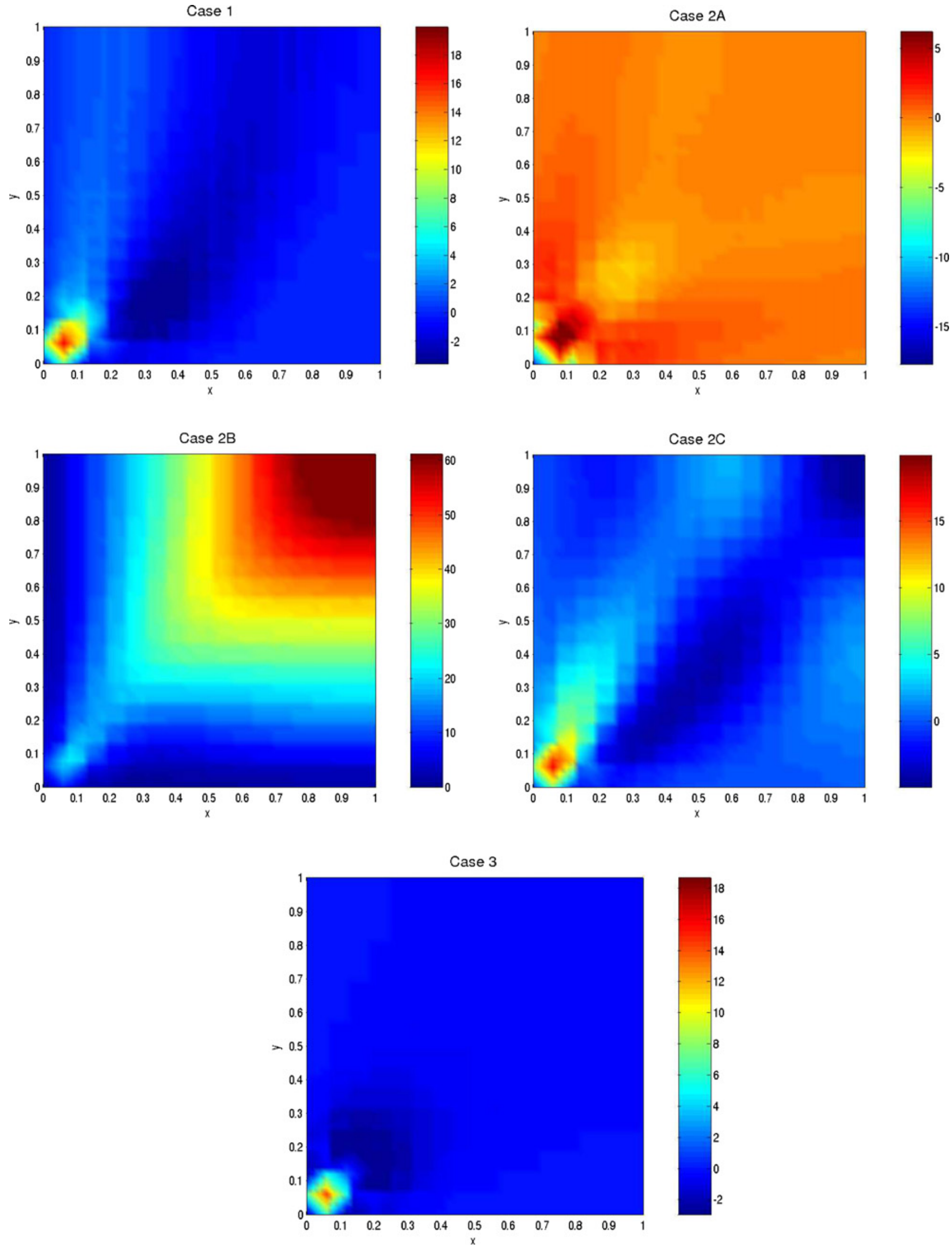

Case 1

Case 2A

Case 2B

Case 2C

Case 3

Fig. 11. The strain field e_{12} in all model cases calculated using the MITC4-S formulation with a uniform 16×16 mesh.

$$\left\{\begin{aligned}
u(x,y) &= \sum_{m,n}\left\{U^A_{mn}\sin\frac{m\pi x}{2}\cos\frac{n\pi y}{2} + U^B_{mn}\cos\frac{m\pi x}{2}\sin\frac{n\pi y}{2}\right\},\\
v(x,y) &= \sum_{m,n}\left\{V^A_{mn}\cos\frac{m\pi x}{2}\sin\frac{n\pi y}{2} + V^B_{mn}\sin\frac{m\pi x}{2}\cos\frac{n\pi y}{2}\right\},\\
w(x,y) &= \sum_{m,n} W_{mn}\cos\frac{m\pi x}{2}\cos\frac{n\pi y}{2},\\
\theta(x,y) &= \sum_{m,n} \Theta_{mn}\sin\frac{m\pi x}{2}\cos\frac{n\pi y}{2},\\
\psi(x,y) &= \sum_{m,n} \Psi_{mn}\cos\frac{m\pi x}{2}\sin\frac{n\pi y}{2}.
\end{aligned}\right. \tag{23}$$

We also observe that the load is not able to excite Fourier modes with m or n even. Consequently, we have to sum over odd indices only in the above expressions. In addition, the coefficients U^B_{mn}, V^B_{mn} vanish if x and y are the principal curvature coordinates which is the case when $c = 0$ in (3). Similarly, U^A_{mn}, V^A_{mn} are dropped when $a = b = 0$, i.e. x and y are the principal curvature coordinates rotated by 90 degrees.

To determine the unknown coefficients, we substitute the Ansatz (23) directly into the expression (4) for the total energy and integrate the strain energy density over one period $\hat{\omega}$ as indicated by the dash line in Fig. 1. The solution is then obtained by choosing

$$\boldsymbol{z}_{mn} = \{U^A_{mn} V^A_{mn} U^B_{mn} V^B_{mn} W_{mn} \Theta_{mn} \Psi_{mn}\}, \tag{24}$$

to make

$$\mathscr{F}(u,v,w,\theta,\psi) = \frac{1}{2}\sum_{m,n}\boldsymbol{z}^T_{mn}\boldsymbol{A}_{mn}\boldsymbol{z}_{mn} - \sum_{m,n}\boldsymbol{z}^{\mathrm{T}}_{mn}\boldsymbol{b} = \min! \tag{25}$$

The symmetric matrix $\boldsymbol{A}_{mn}$ is also positive definite and the load vector $\boldsymbol{b}$ is defined as

$$\boldsymbol{b} = -4F\{0\ 0\ 0\ 0\ 1\ 0\ 0\}. \tag{26}$$

The minimum is achieved if and only if $\boldsymbol{z}_{mn}$ is the solution of the equation

$$\boldsymbol{A}_{mn}\boldsymbol{z}_{mn} = \boldsymbol{b} \tag{27}$$

for every m and n.

We evaluated by symbolic computation the entries of the matrix $\boldsymbol{A}_{mn}$ as functions of the indices m, n and the parameters v, t, a, b, c. Symbolic expansion of the solution $\boldsymbol{z}_{mn}$ is also in the realms of possibility but the expressions become so complicated that their applicability is questionable. However, the numerical values of the Fourier coefficients are easily obtained by giving some values to the parameters and choosing suitable stopping indices for m and n.

4. The case studies

We turn now to numerical experiments and fix the values of the Poisson ratio, shell thickness and the load amplitude by setting

$$v = 0.3, \quad t = 0.01, \quad F = 1. \tag{28}$$

We choose as demonstrative examples the following combinations of the geometry parameters (a,b,c):

Case 1: (1, 0, 0)
Case 2A: (0, 0, 1)
Case 2B: (1, −1, 0)
Case 2C: (2, −1, 0)
Case 3: (1, 1, 0)

We note that all geometric categories of a shell (Fig. 3) are represented in the above model problems: Case 1 is essentially the pinched cylinder problem whereas Cases 2A, B, C stand for hyperbolic geometry with different alignments of the characteristic lines of the midsurface. Finally, Case 3 is an example of an elliptic shell (with no characteristic lines).

In the finite element computations, we model numerically only the unit square $\omega = (0,1)\times(0,1)$ and restrict $\boldsymbol{u} = (u, v, w, \theta, \psi)$ on the boundary by the symmetry/antisymmetry conditions

$$\begin{cases} u = \theta = 0 & \text{at } x = 0, \\ v = w = \psi = 0 & \text{at } x = 1, \\ v = \psi = 0 & \text{at } y = 0, \\ u = w = \theta = 0 & \text{at } y = 1, \end{cases} \tag{29}$$

in the Cases 1, 2B, 2C, 3 and by

$$\begin{cases} v = \theta = 0 & \text{at } x = 0, \\ u = w = \psi = 0 & \text{at } x = 1, \\ u = \psi = 0 & \text{at } y = 0, \\ v = w = \theta = 0 & \text{at } y = 1, \end{cases} \tag{30}$$

in the Case 2A. All numerical experiments will be performed with uniform meshes (Fig. 4).

As a global error indicator we choose

$$\widetilde{\mathscr{E}} = \sqrt{\left|\frac{|||\boldsymbol{u}|||^2 - |||\boldsymbol{u}_h|||_h^2}{|||\boldsymbol{u}|||^2}\right|}, \tag{31}$$

which is very easy to compute and one of the most extensively used (cf. [11,12]). For a standard method $|||\cdot|||_h = |||\cdot|||$ and $\widetilde{\mathscr{E}}$ is equal to the relative error in the energy norm. In case of modified bilinear forms the interpretation can become more complicated, see [12]. Nevertheless, this error measure clearly reflects the quality of approximate solutions to some extent in any case.

As discussed above, the exact value for the shear energy (and hence also for the total energy) is infinity in our benchmark problem. In the numerical convergence studies that follow, we consider only membrane and bending energies by replacing $|||\cdot|||$ in Eq. (31) with the square root of membrane or bending energy for which the reference values are well-defined.

4.1. Experiments with the hp-approach

The following experiments are based on uniform $N\times N$ rectangular subdivisions of ω. In Tables 1 and 2 we measure the relative errors in membrane and bending energies with p ranging from 1 to 8. Here, the total amount of degrees of freedom is kept roughly the same by decreasing N simultaneously. The results illustrate once again very clearly the much better behaviour of standard high-order elements in contrast to low-order ones.

This fact is emphasized even further in Figs. 5–9, where the quality of strain approximations is examined. We show as an example the tangential shear strain $e_{12} = \beta_{12} - \frac{t}{2}\kappa_{12}$

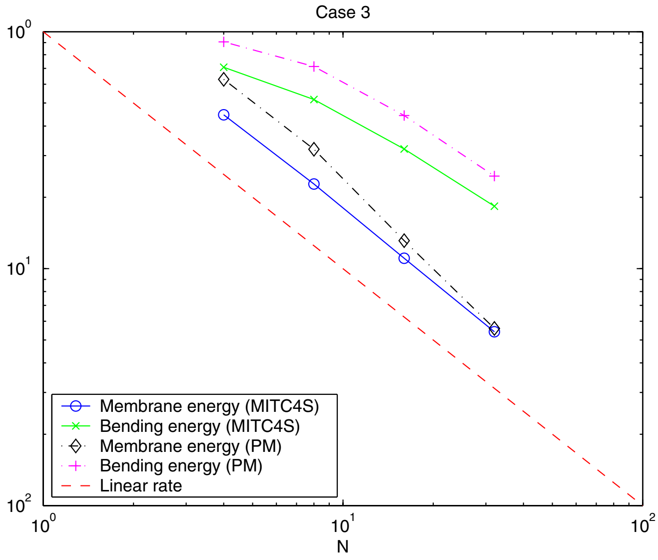

Fig. 12. Comparison between the MITC4-S formulation and the plate-membrane (P-M) element using a sequence of uniform $N\times N$-meshes with $N = 4, 8, 16, 32$.

obtained with p-FEM on a uniform 8×8-mesh along with the reference fields according to the series solution. We conclude that the strains (and also the stresses) are approximated with a feasible accuracy already when $p=4$, while the usability of the results is questionable when $p=1,2$. Eventually, when $p=8$, there arises no discrepancies between the reference and the finite element solution.

Also the theoretical predictions about the layer behaviour are reflected in these results. Strong line layers decay from the characteristic lines of the midsurface in the Cases 1, 2A, 2B and 2C whereas only a "hot spot" around the point load is present in the elliptic Case 3. However, the Case 2B is qualitatively different from the others because the deformation happens to be bending-dominated in that case. Indeed, the load is able to excite non-trivial Fourier modes satisfying the membrane constraints (5) as is easily verified. In the other model cases this is not possible and the strain energy is concentrated asymptotically in the layers, cf. [2].

We finally note that in all our model cases (except in the bending-dominated Case 2B), the displacement field $\boldsymbol{u}$ is approximated very accurately already when $p=2$. Consequently, it is important to use also other error measures than pointwise displacements in a benchmark situation like this.

4.2. Experiments with the MITC4-S algorithm

We determine next what is the response of the best known reduced strain scheme to the model problem. We

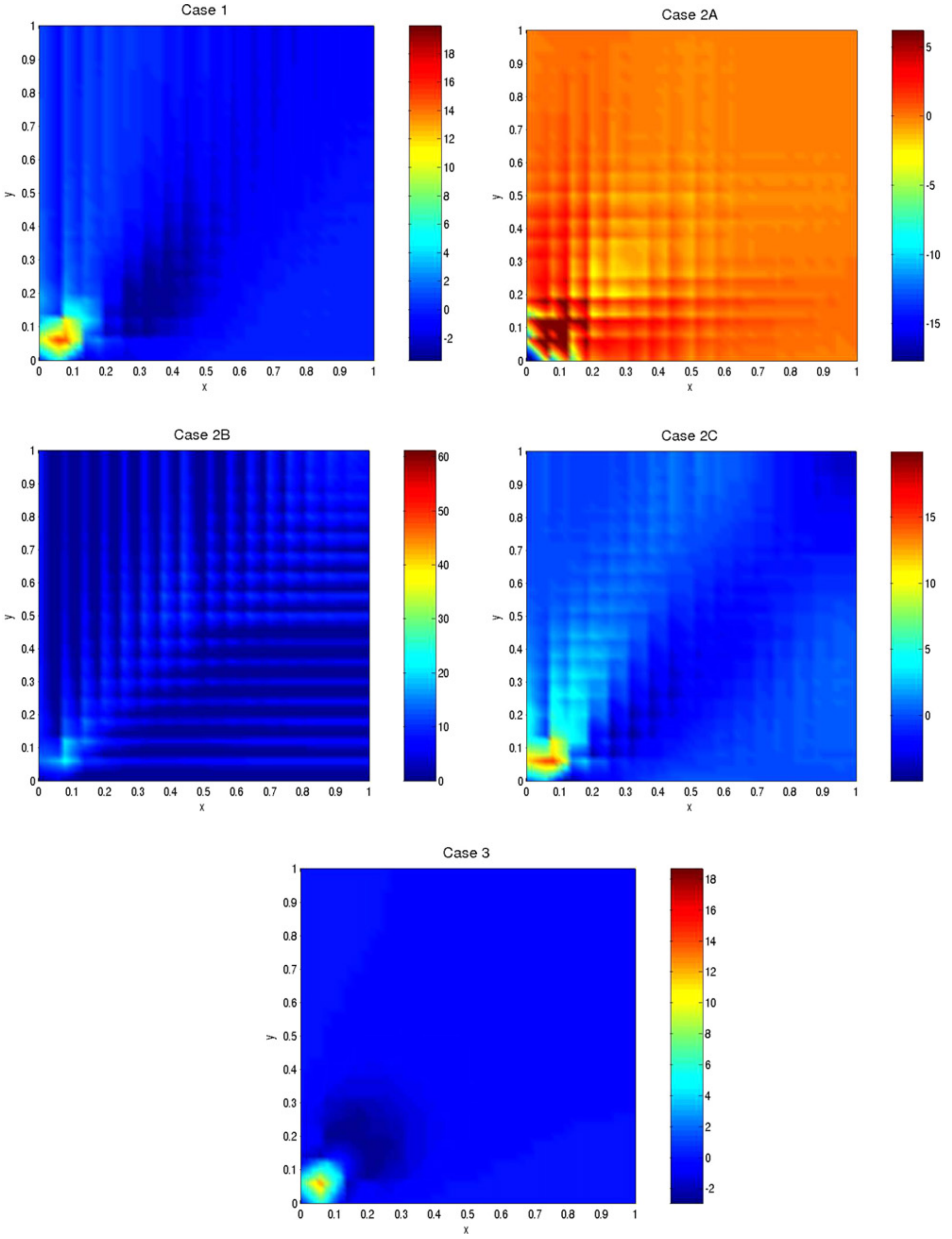

Fig. 13. The strain field e_{12} in all model cases calculated using the plate-membrane element with a uniform 16×16 mesh.

compute the membrane and bending energies on a uniform $N \times N$-mesh with $N = 4, 8, 16, 32$ and check the convergence behaviour with respect to the error indicator $\widetilde{\mathscr{E}}$. The results are shown in Tables 3 and 4 and visualized on a logarithmic scale in Fig. 10.

Best accuracy is obtained in the pure bending situation 2B. This is to be expected, since the modifications (12) and (13) are aimed for preventing membrane and shear locking caused by the asymptotic constraints (5) and (6) in the first place. In case of the layer modes, the asymptotic constraints are of more complicated nature as they are enforced anisotropically depending on the direction of the decay of the layer mode [9]. Nevertheless, the strain reductions seem to improve accuracy considerably in any case and the results are competitive even against the *hp*-approach. This is confirmed also in Fig. 11 where we show again the strain field e_{12} in the model cases, but now computed with the MITC4-S algorithm on a 16×16-mesh.

4.3. Does the plate-membrane element work?

Let us finally examine whether it is possible to approximate the layer modes accurately without modifying the membrane strains β_{ij}. This question is motivated also by the analysis of [9] which shows that the dominant locking effects are due to the shear constraints (6) as regards to the main layer modes. In fact, membrane constraints do not arise at all in the most common layer mode with $n = 2$, so one might expect that at least in that case the plate-membrane element would work as well as MITC4-S, or perhaps better.

So let us compute once more the strain field e_{12}, this time leaving the membrane strains untouched (Fig. 13). The conclusion from the experiments is that when approximating the line layers with $n = 3, 4$ in parabolic and hyperbolic geometries, merely the shear modification (13) is not sufficient to unlock the standard bilinear scheme. In the bending-dominated situation 2B a complete failure results as expected.

Case 3 is now the most interesting one since the deformation field consists almost purely of a point layer decaying radially from the load application point. Even here MITC4-S still produces a solution of slightly better quality – somewhat unexpectedly. On the other hand, the convergence rate with respect to the error indicator (31) seems to be better when the membrane strains are left unmodified as indicated by Fig. 12.

References

[1] J. Pitkäranta, The problem of membrane locking in finite element analysis of cylindrical shells, Numer. Math. 61 (1992) 523–542.

[2] J. Pitkäranta, Y. Leino, O. Ovaskainen, J. Piila, Shell deformation states and the finite element method: a benchmark study of cylindrical shells, Comput. Methods Appl. Mech. Engrg. 128 (1995) 81–121.

[3] H. Hakula, Y. Leino, J. Pitkäranta, Scale resolution, locking and high-order finite element modelling of shells, Comput. Methods Appl. Mech. Engrg. 133 (1996) 157–182.

[4] K. Gerdes, A.M. Matache, C. Schwab, Analysis of membrane locking in *hp* FEM for a cylindrical shell, Z. Angew. Math. Mech. 78 (1998) 663–686.

[5] M. Malinen, On the classical shell model underlying bilinear degenerated shell finite elements, Int. J. Numer. Meth. Engrg. 52 (2001) 389–416.

[6] M. Malinen, On the classical shell model underlying bilinear degenerated shell finite elements: general shell geometry, Int. J. Numer. Meth. Engrg. 55 (2002) 629–652.

[7] V. Havu, J. Pitkäranta, Analysis of a bilinear finite element for shallow shells I: Approximation of inextensional deformations, Math. Comput. 71 (2002) 923–943.

[8] V. Havu, J. Pitkäranta, Analysis of a bilinear finite element for shallow shells II: Consistency error, Math. Comput. 72 (2003) 1635–1653.

[9] J. Pitkäranta, A.-M. Matache, C. Schwab, Fourier mode analysis of layers in shallow shell deformations, Comput. Methods Appl. Mech. Engrg. 190 (2001) 2943–2975.

[10] D. Chapelle, K.-J. Bathe, The Finite Element Analysis of Shells: Fundamentals, Springer, Germany, 2003.

[11] K.-J. Bathe, A. Iosilevich, D. Chapelle, An evaluation of the MITC shell elements, Comput. Struct. 75 (2000) 1–30.

[12] M. Malinen, J. Pitkäranta, A benchmark study of reduced-strain shell finite elements: quadratic schemes, Int. J. Numer. Meth. Engrg. 48 (2000) 1637–1671.